Fundamental Understanding of "Fresh" Lithium Nucleation and Growth in Sulfide-Based Anode-Free Solid-State Batteries: Effects of Substrate, Current Density, and Li$^+$ Supply

*Jiwei Wang, Yuzi Liu, Mengting Ye, Guanyi Wang, Cheng Xu, and Hongli Zhu**

Understanding the electrochemical extraction and deposition of lithium (Li) from cathode is crucial for advancing anode-free solid-state batteries (AFSSBs). Herein, cryo-transmission electron microscopy (cryo-TEM) and electrochemical studies are employed to investigate how current collector surface properties, current densities, and cathode loadings influence the morphology of fresh electrochemically deposited Li and the electrochemical performance in sulfide-based AFSSBs. Cryo-TEM reveals that Cu current collectors induce irregular, dendritic Li deposits due to their lithiophobic nature and reactivity with $Li_{5.4}PS_{4.4}Cl_{1.6}$ (LPSC), while Ni and Au facilitate more uniform, planar-like Li growth. The morphology of the deposited Li also depends on current density: higher rates produce smaller, porous particles versus larger, denser deposits at lower rates. Importantly, for the first time, we discovered that low cathode loadings lead to poor cycling stability due to insufficient Li$^+$ supply for complete anode coverage, contrary to conventional solid-state batteries with preloaded Li metal anodes. This finding establishes a design principle where adequate cathode Li$^+$ reservoirs are essential for anode interface stability in AFSSBs. Overall, this work elucidates the interplayed effect of current collectors, current densities, and cathode loadings on Li morphology and cycle stability, offering fundamental insights into cathode-derived Li behavior and practical guidelines for optimizing AFSSBs performance through nucleation control and interface engineering.

1. Introduction

The global imperative for sustainable energy solutions has positioned all-solid-state batteries (ASSBs) at the forefront of next-generation energy storage innovation. Among various solid electrolyte (SE) systems, sulfide solid electrolytes, such as argyrodites like Li_6PS_5Cl, offer high room-temperature ionic conductivities approaching 10^{-2} S cm^{-1},[1,2] enabling cell-level energy densities of ≈400 Wh kg^{-1} when paired with a Li metal anode. Therefore, these sulfide-based all-solid-state batteries offer exceptional potential for safe, high-energy-density storage systems.[3,4] However, their commercialization remains challenging due to the Li dendrite formation, high reactivity of Li, and the difficulty of fabricating ultrathin, high-purity Li foils (<20 μm) using scalable and low-cost methods, which hinder long-term cycling stability, cost-effective manufacturing, and commercial viability.[5,6]

To address these challenges, anode-free solid-state batteries (AFSSBs) have emerged as a promising alternative, eliminating the usage of pre-existing Li anodes and providing a unique platform for fundamentally investigating the in situ electrochemically deposited "fresh Li".[7,8] Unlike pre-existing bulk Li, this newly electrochemically deposited "fresh Li", originating from the cathode, exhibits unique characteristics in its nucleation mechanism, growth behavior, and interfacial dynamics that fundamentally influence battery performance. Understanding the behavior of this electrochemically deposited fresh Li is essential for achieving stable cycling and high energy density in AFSSBs.

Despite their promising advantages, AFSSBs face critical performance limitations, primarily rapid capacity fade stemming from inefficient Li deposition/stripping processes and dead Li formation, which lead to abnormally low initial coulombic efficiency (ICE).[9,10] The interplay between current collector (CC) properties, applied current density, and cathode mass loading significantly influences AFSSB performance and fresh Li behavior. While researchers have explored various current collector

---

J. Wang, M. Ye, C. Xu, H. Zhu
Department of Mechanical and Industrial Engineering
Northeastern University
360 Huntington Avenue, Boston, Massachusetts 02115, USA
E-mail: h.zhu@neu.edu

Y. Liu, G. Wang
Center for Nanoscale Materials
Argonne National Laboratory
9700 South Cass Avenue, Lemont, Illinois 60439, USA

The ORCID identification number(s) for the author(s) of this article can be found under https://doi.org/10.1002/smll.202506473

DOI: 10.1002/smll.202506473

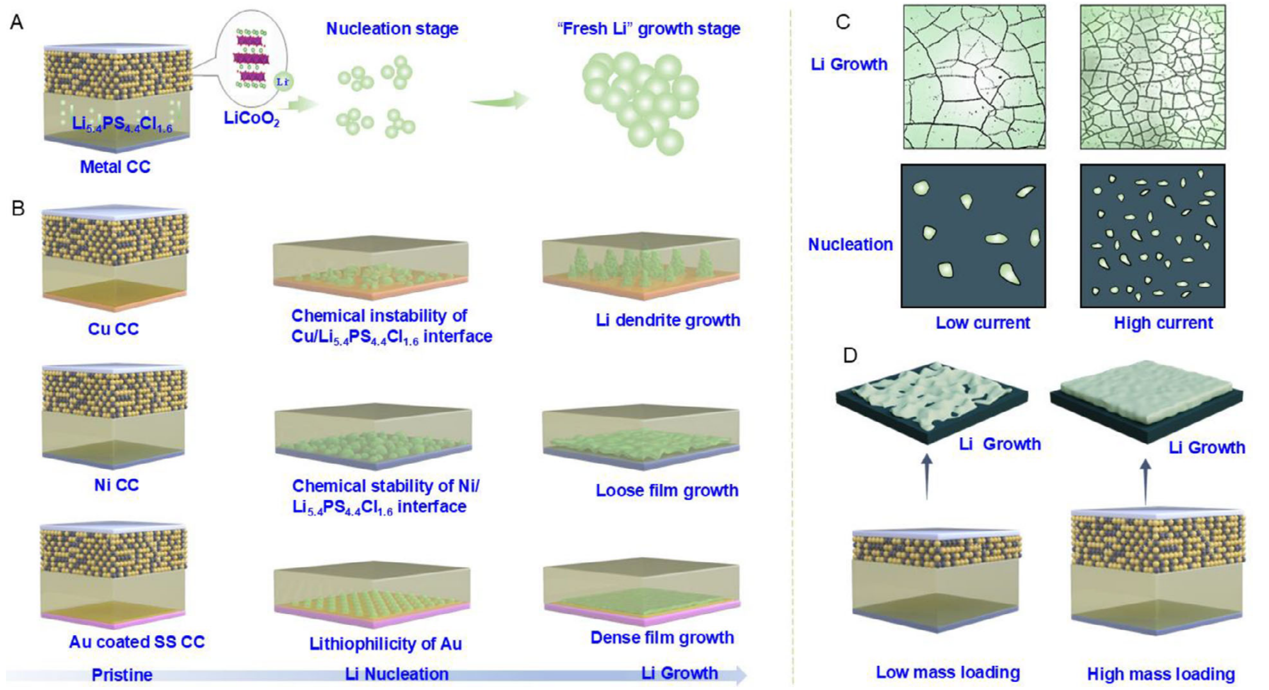

Figure 1. A) Schematic of "fresh Li" formation procedure in a sulfide-based anode-free solid-state battery (AFSSB). The black balls represent the LiCoO$_2$ active materials, the yellow balls represent the Li$_{5.4}$PS$_{4.4}$Cl$_{1.6}$ SE, and the green balls represent the Li ion (Li$^+$). B) The schematic of Li nucleation and growth processed on different substrates (Cu, Ni, and Au-coated SS). C) The effects of low and high current density on Li nucleation and growth. D) The effects of low and high cathode mass loading on the Li coverage in the anode side.

modifications to enhance performance,[11–18] fundamental questions remain unanswered regarding how these factors influence Li nucleation and growth at the nanoscale, particularly at the critical Li/SE interface. Furthermore, the relationship between operating parameters (current density and cathode mass loading) and Li deposition morphology and uniformity in sulfide-based systems remains poorly understood, especially considering the inherent chemical-, mechanical-, and electrochemical- instabilities at the Li/sulfide electrolyte interface.

To address these critical knowledge gaps and gain crucial new insights into fresh Li behavior, we employ Li$_{5.4}$PS$_{4.4}$Cl$_{1.6}$ (LPSC) as a solid electrolyte to investigate the complex mechanisms governing Li deposition in sulfide-based AFSSBs. Using a combination of electrochemical methods and ex situ cryo-transmission electron microscopy (cryo-TEM), we comprehensively explore three critical parameters affecting fresh Li deposition: current collector, current density, and cathode mass loading. Our study addresses fundamental questions regarding 1) the influence of surface properties of the current collector on fresh Li nucleation and morphology, 2) the role of current density in determining deposit structure and distribution, and 3) the impact of cathode mass loading on Li coverage and cycling stability. By elucidating the interplay between these factors and the unique properties of fresh Li, our work provides a comprehensive understanding of fresh Li deposition behavior in sulfide-based AFSSBs.

2. Results and Discussion

The fundamental understanding of Li nucleation and crystal growth mechanisms in electrodeposition processes is central to advancing AFSSB technology. **Figure 1A** presents a schematic illustration of "fresh Li" formation in sulfide-based AFSSBs, depicting a crucial electrochemical process where Li ions are systematically extracted from lithium-layered oxide cathodes and electrodeposited onto a pristine current collector during initial charging. This unique phenomenon can be divided into three distinct phases: initial nucleation, crystal growth, and bulk formation. During the critical initial charging stage, Li nucleation occurs on the bare current collector surface, establishing discrete nucleation sites that serve as foundation points for subsequent growth. These initial nuclei then undergo progressive crystal growth, eventually coalescing into substantial Li metal deposits. The absence of a pre-existing Li reservoir at the anode position makes this nucleation and early-stage crystal growth process particularly significant, as it fundamentally determines both the quality of the resultant Li metal layer and the long-term cycling performance of the AFSSBs.

To systematically investigate this complex process, in this study, we have identified three critical parameters that govern Li deposition behavior in sulfide-based AFSSBs, as illustrated in Figure 1B–D. First, we examine how current collectors (CCs) with different surface properties influence initial Li nucleation sites, growth patterns, and interfacial properties (Figure 1B). Second, we analyze how varying current densities affect Li deposition morphology and spatial distribution (Figure 1C). Third, we investigate how cathode material loading impacts Li deposition uniformity and coverage on the current collector surface (Figure 1D). This study enables a comprehensive understanding of the interrelationships between these key parameters and their collective impact on fresh Li formation and evolution in sulfide-based AFSSBs.

2.1. Effect of the Surface Properties of the Current Collector on Li Nucleation and Growth

To better understand the influence of the surface properties of the current collectors on Li nucleation and growth in sulfide-based AFSSBs, we analyzed the early-stage Li morphologies plated on different current collectors using cryo-TEM. Anode-free solid-state full cells were assembled with a $LiCoO_2$ (LCO) cathode as the Li source and TEM grids (Cu, Ni, and Au mesh) as anode current collectors. LCO was chosen as a model cathode for its superior electrochemical kinetics, ensuring that Li deposition behavior in the full cell is not affected by the sluggish kinetics of the cathode. Cryo-TEM samples were prepared by depositing a controlled amount of Li directly onto the different metal mesh grids within a standard pressurized cell. The metal grid with the deposited Li was then loaded into the TEM column by a Cryo-transfer TEM holder (Figure S1, Supporting Information), with the entire process conducted under liquid nitrogen cryogenic temperature to preserve the native structure of highly sensitive Li. To capture early-stage Li formation, we precisely controlled the plating amount by charging the LCO to 15% state of charge (SOC) (equivalent to 0.5 mAh cm^{-2} Li) at 0.25C (Figure S2, Supporting Information).

Figure 2A,B show cryo-TEM images of Li deposits formed on the Cu grid. The Li metal particles present irregular morphologies with different shapes. Although non-dendrite-like morphology, such as ball-like structure composed of numerous small particles (Figure 2A), was observed, most Li metal particles examined from different regions display a hybrid mossy-like and dendrite morphologies (Figure 2B; Figure S3, Supporting Information). Although previous research has studied the interface reactions between LPSC and Li metal,[19] the interfacial chemistry between the freshly plated Li and LPSC in anode-free full cells remains poorly understood, particularly with Cu CCs, which show inherent instability with LPSC.[20] To elucidate the chemical composition of these Li deposits, we conducted cryogenic scanning transmission electron microscopy (cryo-STEM) imaging (Figure 2G). The high-angle annular dark-field STEM (HAADF-STEM) image reveals a bright contrast near the Cu filament, while the dendrite filaments far from the Cu filament exhibit relatively dark contrast. A previous study demonstrated that the Li dendrites appear darker contrast than the SEI in HAADF image mode due to Li having smaller scattering.[21] The bright contrast observed in the dendrite filaments (indicated by the red arrow) indicates the occurrence of side reactions between deposited Li and SE. This inference is supported by the distribution of S and Cl signals in STEM-energy dispersive spectroscopy (EDS) mapping, where the highest intensities coincide with the bright contrast areas near the Cu filament in the HAADF image. Notably, unlike the conformal SEI coating formed on Li metal in previous studies,[22,23] this side reaction-induced SEI in AFSSBs forms non-uniformly on the Li filament, potentially explaining the poor electrochemical cycling performance. The oxygen signal's morphology closely matches the HAADF image, confirming the presence of Li metal, as Li's high reactivity makes it the only component in the sample capable of introducing the O signal.[24,25] Most significantly, we detected Cu signals in both the Cu filament wire and Li filaments, with high Cu intensity observed at area 2 (Figure S4, Supporting Information), indicating substantial Cu degradation through reactions with the solid electrolyte. Although Cu is a widely used commercial anode current collector, these findings demonstrate its unsuitability for sulfide-based AFSSBs, consistent with recent studies showing LPSC-induced Cu corrosion forming Cu_2S byproducts.[20] The EDS results, along with the cryo-STEM mapping images of P, S, and Cl, suggest that the interfacial reaction products primarily contain small amounts of S-based species and are enriched in Cl-based species, most likely in the form of Li_2S and LiCl.[19]

In contrast to Cu, Li deposits on Ni CCs exhibit favorable non-dendritic, loose film-like morphologies, suggesting superior plating behavior. As shown in Figure 2C,D, these distinctive morphological characteristics differ markedly from the dendrite-prone deposits observed on the Cu grid. Although the deposit thickness varies across different Ni filaments (Figure S5, Supporting Information), the consistent absence of dendritic structures indicates uniform Li plating behavior on the Ni grid. The oxygen signal morphology's close correspondence with the HAADF-STEM confirms the presence of Li metal. Notably, no Ni signal was detected in the Li filament areas, suggesting the stability of Ni metal in LPSC-based AFSSBs. Cryo-STEM-EDS mappings of S and Cl (Figure 2H), along with EDS results (Figure S6, Supporting Information), reveal that the interface side reaction products are rich in LiCl with minor Li_2S formation, consistent with the findings for the Cu grid. This observation is further validated by scanning electron microscopy (SEM)-EDS analysis over larger detection areas (Figure S7, Supporting Information), which confirms the predominance of Cl-based species in interfacial reactions.

Most notably, the Li deposit on Au CCs reveals a unique two-layer structure: a LiAu alloy layer forms first, followed by distinct dome-shaped Li deposits. As shown in Figure 2E,F, we observed a thin film on the Au filament (marked by orange dashed lines) with an additional thin, dome-shaped deposit of lighter contrast on its outermost layer (indicated by white arrow). The charging voltage plateau at 3.77 V for Au-based cells, significantly lower than cells with Cu and Ni grids (Figure S2, Supporting Information), provides strong evidence for LiAu alloy formation. Thus, we hypothesized that the thin film layer with darker contrast corresponds to a LiAu alloy layer, while the outermost dome-shaped deposits are plated Li. To confirm this, we conducted cryo-STEM-EDS analysis. The morphology of the O signal closely matches the HAADF-STEM image (Figure 2I), indicating that the outermost layer deposits are plated Li. Moreover, the EDS spectra at the film region (area 2 in Figure S8, Supporting Information) showed both Au and O elements, while only O was detected in the outermost layer (area 3 in Figure S8, Supporting Information), further supporting our hypothesis that the outer surface thin layer is Li, and the inner film is a LiAu alloy layer. Cryo-STEM-EDS mappings of Cl (Figure 2I), along with EDS results (Figure S8, Supporting Information), reveal that the interface reaction products are rich in Cl-based species.

Cryo-TEM analysis revealed that the surface properties of the current collector critically influence Li nucleation and growth in sulfide-based AFSSBs. To demonstrate how the surface properties of the current collector, such as chemical stability with LPSC

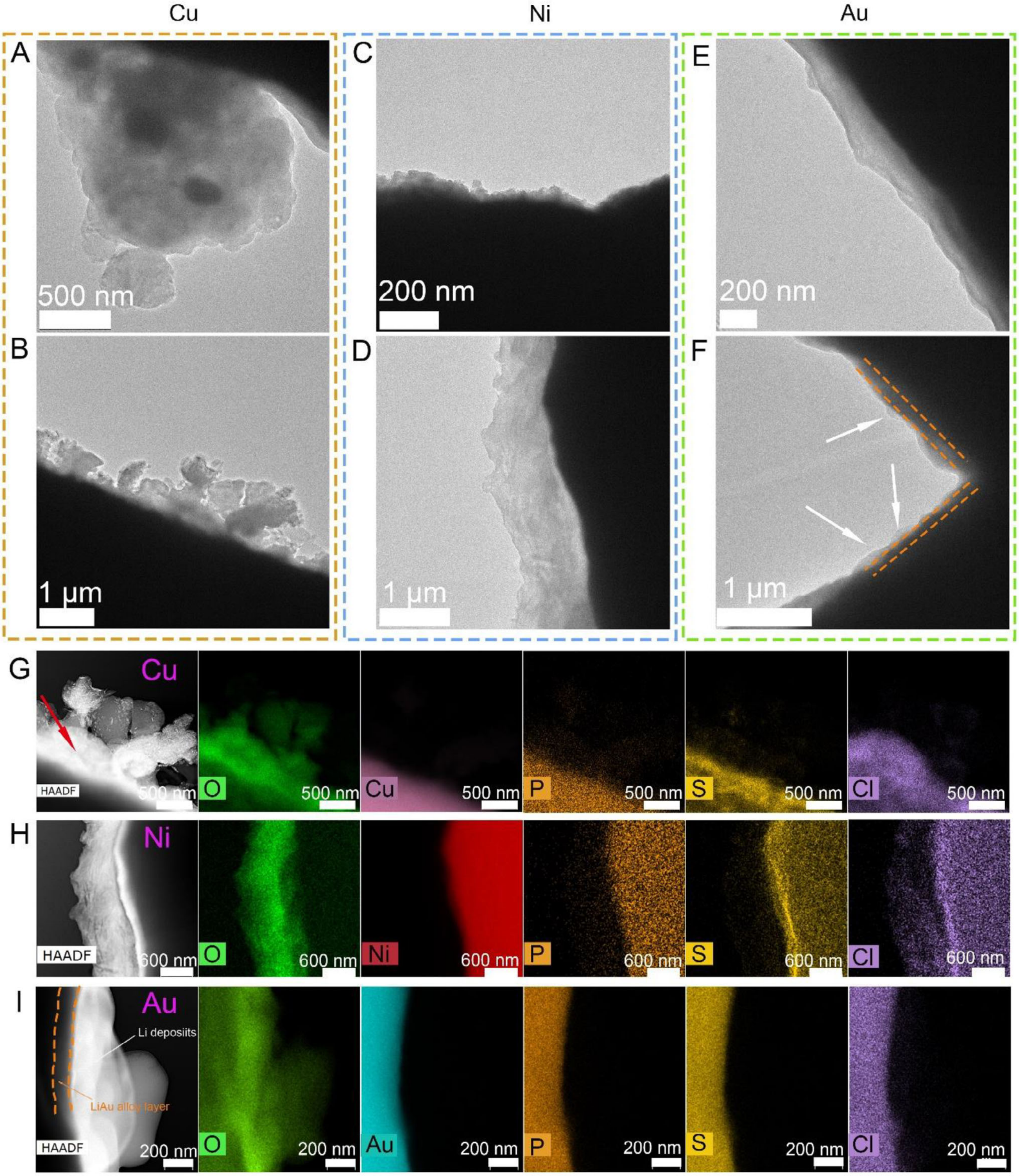

Figure 2. Cryo-TEM characterization of the deposited Li on different current collectors. A,B) Cryo-TEM images of the deposited Li on the Cu grid; C,D) Cryo-TEM images of the deposited Li on the Ni grid; E,F) Cryo-TEM images of the deposited Li on the Au grid; G–I) Cryo-HAADF-STEM images and EDS mapping of the Li deposits on the Cu, Ni, and Au grids, respectively.

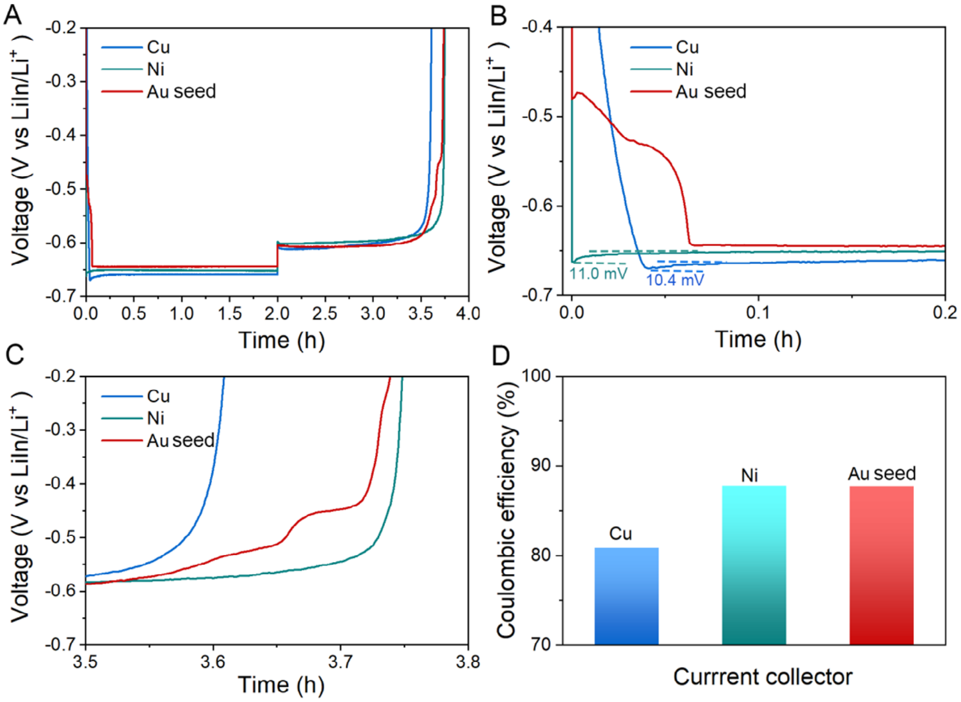

Figure 3. Electrochemistry of anode-free solid-state half-cells using different current collectors. A) Galvanostatic plating/stripping of Li in half-cells with Cu foil, Ni foil, and Au-coated SS foil. Li was plated and stripped at a current density of 0.25 mA cm^{-2} with an areal plating capacity of 0.5 mAh cm^{-2} at room temperature. B) Magnified view of early-stage Li deposition voltage curves showing the nucleation step. C) Magnified view of the end of stripping voltage curves. D) Initial coulombic efficiency comparison of half cells with Cu foil, Ni foil, and Au-coated SS foil current collectors.

SE and Li affinity, influence the electrochemistry in sulfide-based AFSSBs, galvanostatic charge/discharge cycling was conducted on anode-free solid-state half-cells using different types of current collectors. Cu foil, Ni foil, and stainless steel (SS) foil were used as baseline CCs as they are commonly utilized as current collectors in AFSSBs. Although Au foil demonstrates superior chemical stability and lithophilicity toward Li, its high cost restrains its practical application in AFSSBs. Therefore, SS coated with a 20 nm Au seed layer was used as a lithiphilic current collector, which can effectively reproduce the favorable characteristic of Au while substantially reducing the noble metal consumption for pratical application. LPSC was used as the SE, and indium-lithium (InLi) alloy was used as the counter electrode to mitigate side reactions at the counter electrode/LPSC interface. The working electrodes consisted of 20 µm metal foils of the respective CC materials. Half cells were cycled at 0.25 mA cm^{-2} with a fixed capacity of 0.5 mAh cm^{-2}. **Figure 3A** compares the first cycle voltage profiles of the three half-cells. Cu and Ni CCs exhibit significant nucleation overpotentials of 10.4 and 11.0 mV, respectively, while the Au-coated SS CC shows a negligible nucleation overpotential (Figure 3B). Moreover, Li deposition behavior on an SS CC was also examined, revealing a similar behavior to the cell with the Ni CC, where Li undergoes a nucleation overpotential followed by a flat deposition plateau (Figure S9, Supporting Information). Therefore, the negligible nucleation overpotential on Au-coated SS is primarily attributed to the 20 nm Au seed layer, whose high Li affinity effectively reduces the Li nucleation overpotential. The cell with Au-coated SS displays two distinct alloy plateaus at −0.48 and −0.54 V (vs InLi/Li$^+$) before Li nucleation and growth stages, indicating the formation of Li-Au alloys.[26,27] Despite similar nucleation overpotentials, the Cu CC cell exhibits a larger Li deposition overpotential of 39.0 mV compared to the Ni CC cell (30.0 mV), suggesting higher interfacial resistance during Li deposition. In contrast, Au-coated CCs show the lowest Li deposition overpotential of 24.7 mV, indicating the smallest interfacial resistance among the three. All the cells were assembled with the thickness of the SE pellets the same by maintaining a consistent SE powder loading of 100 mg cm^{-2}, ensuring that variations in deposition overpotential are not influenced by SE thickness. Additionally, to mitigate cell-to-cell variations, we tested multiple cells for each substrate (Figure S10, Supporting Information), reinforcing the reliability of our observations. The Au alloying process fundamentally alters the Li deposition mechanism by creating energetically favorable nucleation sites, effectively eliminating the nucleation barrier observed with Cu and Ni. The subsequent lower deposition overpotential on Au suggests that the formed Li-Au alloy interlayer facilitates charge transfer and Li-ion transport at the interface, potentially through modified lithiophilic properties, electronic structure, and enhanced surface conductivity.

The stripping behavior also varies significantly among the CCs (Figure 3C). The Cu CC cell shows an abrupt termination of the stripping process at ≈3.6 h, accompanied by a sharp voltage increase, indicating a complete depletion of active Li. The Ni CC cell exhibits a more gradual sloping stripping potential, terminating ≈3.75 h. For the Au-coated SS CC, two voltage plateaus appear after Li metal stripping, corresponding to LiAu de-alloying processes. These divergent plating/stripping behaviors result in varying coulombic efficiencies (CEs), as shown in Figure 3D. The Cu CC cell demonstrates a lower CE of 80.2%, while Ni and Au-coated SS CC cells achieve higher CEs of ≈87.8%. This analysis reveals the critical role of the surface properties of the metal CC in optimizing the electrochemical performance of sulfide-based AFSSBs, with Au-coated SS and Ni CCs showing superior characteristics for fresh Li deposition and stripping efficiencies.

2.2. Effect of Current Density on Li Nucleation and Growth

To elucidate the influence of current density on the Li nucleation and growth on metal CC in sulfide-based AFSSBs, cryo-TEM was employed to examine the morphologies of Li deposits at a low current density of 0.04C. Figure S11 (Supporting Information) presents the galvanostatic charge profiles of the anode-free full cells cycled at 0.04C. All cells were charged to 15% SOC, ensuring that the same amount of Li was deposited as in the higher current density condition of 0.25C. Compared to Li plated at 0.25C (**Figure 4**A; Figure S12A, Supporting Information), most of the Li plated at 0.04C exhibits a nanowire-shaped morphology, with dendritic filaments that have denser microstructure (Figure 4B; Figure S12B, Supporting Information). Additionally, a few nanoplate-shaped Li dendrites with dense structures were observed (Figure S13, Supporting Information). Cryo-STEM-EDS mapping of Cu (Figure 4G) shows a similar signal distribution to that observed at 0.25C, indicating that side reactions involving Cu and the SE are consistent. Chlorine (Cl) and sulfur (S) mapping images also suggest that the side reaction products are consistent with those observed at 0.25C (Figure 2G).

Figure 4D and Figure S12D (Supporting Information) display cryo-TEM images of Li deposits on the Ni grid. In contrast to the Li deposited at 0.25C (Figure 4C; Figure S12C, Supporting Information), the Li plated at 0.04C presented a uniform dome-shaped morphology with a dense structure. Moreover, the Li particle size at 0.04C ranged from 100 to 200 nm, which is larger than the 20–40 nm size observed at 0.25C. Cryo-STEM-EDS mapping images of Ni, S, and Cl (Figure 4H) show similar results to those observed at 0.25C (Figure 2H).

Cryo-TEM images of Li deposits on an Au grid at 0.04C are shown in Figure 4F and Figure S12F (Supporting Information). A 150 nm film formed on the Au filament, as marked by the orange dashed lines, which is the LiAu alloy layer. Additionally, a thin, dome-shaped Li deposit with lighter contrast was observed on the outermost layer of the 150 nm film, indicated by the white arrow. Figure 4E and Figure S12E (Supporting Information) display Cryo-TEM images of Li deposits on an Au grid at 0.25C, showing similar deposition morphology to that observed at 0.04C. However, the LiAu alloy layer at 0.25C was more porous and thinner compared to the 0.04C deposit. This is likely because, at a higher current rate, more Li ions accumulate on the surface, leading to a faster saturation of the Au layer with Li near the surface, followed by earlier Li plating on the outer surface of the saturated Au layer. Cryo-STEM-EDS mapping images of Li deposits on Au grid (Figure 4I) show similar results to those observed at 0.25C (Figure 2I).

To demonstrate the dependence of Li nucleation on current density and its influence on subsequent Li growth on metal CCs, galvanostatic charge/discharge experiments were conducted on LiIn/LPSC/metal CC half-cells under varying current densities. **Figure 5**A presents the initial plating/stripping profiles of Cu-based AFSSBs at current densities of 0.25 and 0.05 mA cm^{-2}, while Figure 5B zooms in on the Li nucleation stage. At higher current densities, a noticeable nucleation potential lag and larger overpotential for subsequent Li growth were observed. Although the stripping efficiency was comparable at both current densities, the stripping plateau showed an earlier slope at high current density, indicating increased interfacial resistance toward the end of stripping. Similar behavior was observed with Ni CC (Figure 5C,D) and Au CC (Figure 5E,F) based anode-free half-cells, where higher current densities also led to a nucleation potential lag and larger overpotential for Li growth. These differences in nucleation potential and growth overpotential are closely related to the Li nucleation density and the subsequent morphologies of Li deposition.[28–31] These results can be well aligned with the early-stage Li morphologies under different current densities from cryo-TEM.

The above current density effects on Li nucleation and growth reveal fundamental correlations between applied current and electrodeposition behavior across Cu, Ni, and Au CCs. At higher current densities (0.25 mA cm^{-2}), all substrates exhibit pronounced nucleation potential lags and elevated growth overpotentials compared to lower current densities (0.05 mA cm^{-2}), reflecting increased kinetic barriers for nuclei formation and growth under higher current. This suggests a fundamental relationship between current density and Li^{+} ion supersaturation at the electrode interface, directly influencing nucleation site density and subsequent growth morphologies. The observation of the earlier onset of voltage slope increases during stripping at high current densities, despite similar stripping efficiencies, indicates the formation of isolated Li domains and deteriorating electrical contact—a critical insight into interface evolution during cycling. These findings demonstrate that current density not only governs initial nucleation energetics but also fundamentally determines the entire deposition process through its impact on nucleation density, growth patterns, and interfacial dynamics, providing crucial guidelines for optimizing AFSSBs operating conditions.

2.3. Impact of Cathode Areal Mass Loading on the Li Anode Stability in Anode-Free Batteries

In anode-free batteries, Li-containing cathodes are the sole source of Li ions during cycling. Therefore, cathode mass loading plays a critical role in determining the electrochemical performance of an anode-free full cell. Previous studies have shown that low cathode mass loading can ensure excellent long-term stability in solid-state Li-metal batteries due to the minimal volume variation on the anode side.[32] However, it remains unknown how the cathode mass loadings (Li^{+} supplier) affect the Li growth in solid-state anode-free batteries. According to our studies in Section 2.2, in AFSSBs, the “freshly” plated Li tends to exhibit irregular morphologies, making it difficult to achieve uniform coverage on the metal CC. A reduced amount of Li from the cathode may worsen this effect, leading to incomplete Li coverage with voids on the CC. To investigate the impact of cathode mass loading on cycling stability, we tested sulfide-based AFSSBs with varying cathode mass loadings. The cycling stability confirmed our

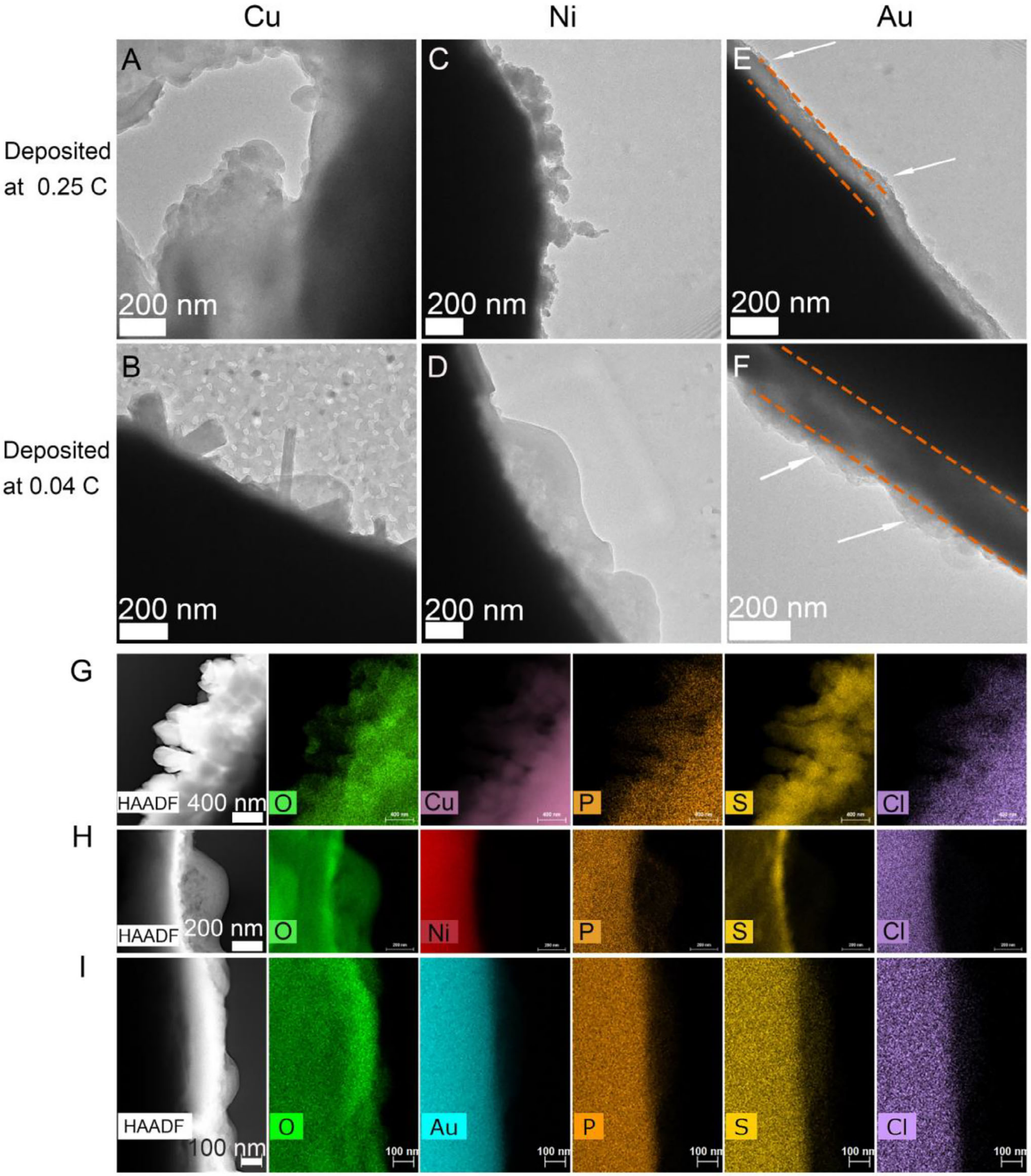

Figure 4. Cryo-TEM characterization of the deposited Li under different current densities. A,B) Cryo-TEM images of the deposited Li on the Cu grid at 0.25 and 0.04C, respectively; C,D) Cryo-TEM images of the deposited Li on the Ni grid at 0.25 and 0.04C, respectively; E,F) Cryo-TEM images of the deposited Li on the Au grid at 0.25 and 0.04C, respectively; G–I) Cryo-HAADF-STEM images and EDS mapping of the Li deposits on the Cu, Ni, and Au grids at 0.04C, respectively.

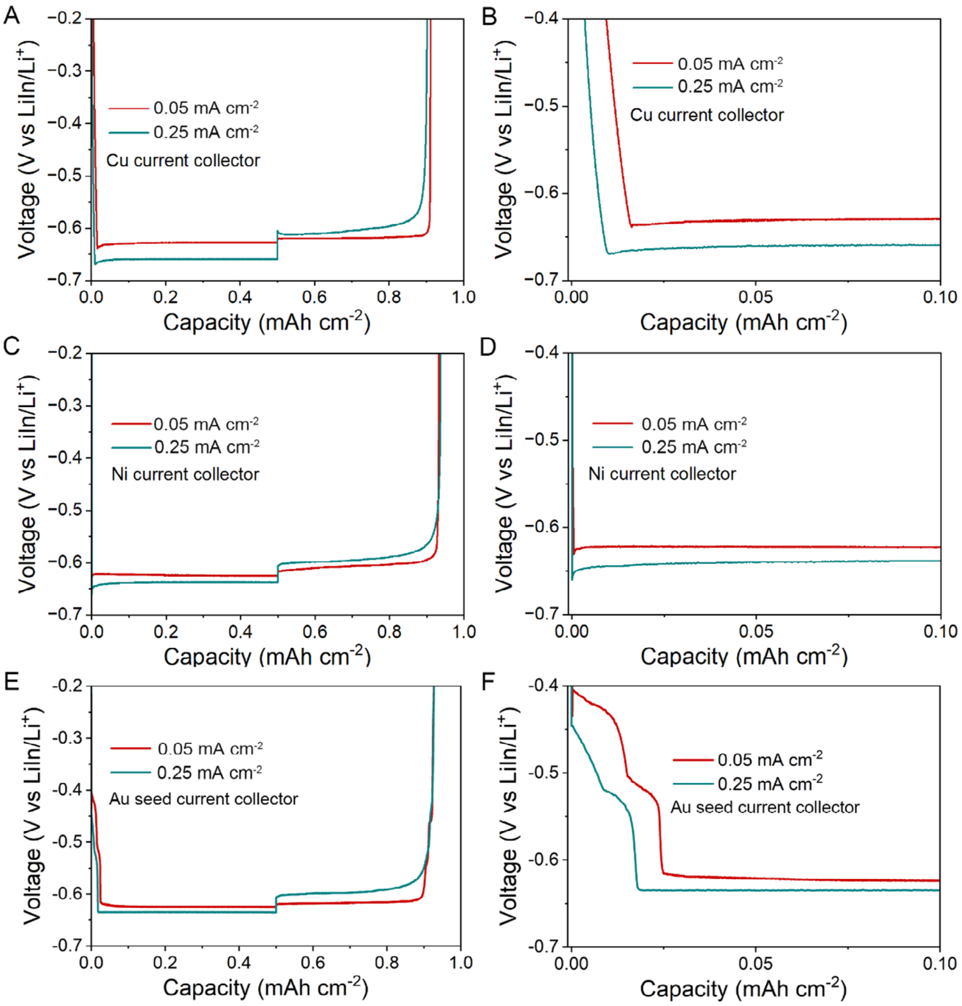

Figure 5. Electrochemistry of anode-free solid-state half-cells using different current densities. A) Galvanostatic plating/stripping of Li in half-cells with Cu at 0.05 and 0.25 mA cm^{-2}. B) Magnified view of early-stage Li deposition (in Figure A) voltage curves showing the nucleation step. C) Galvanostatic plating/stripping of Li in half-cells with Ni at 0.05 and 0.25 mA cm^{-2}. D) Magnified view of early-stage Li deposition (in Figure C) voltage curves showing the nucleation step. E) Galvanostatic plating/stripping of Li in half-cells with Au seed at 0.05 and 0.25 mA cm^{-2}. F) Magnified view of early-stage Li deposition (in Figure E) voltage curves showing the LiAu alloy and Li nucleation step. All cells were fixed with an areal Li plating capacity of 0.5 mAh cm^{-2}.

expectations: the cell with the lowest cathode mass loading exhibited the fastest capacity decay, while capacity retention improved as cathode mass loading increased.

Galvanostatic charge/discharge profiles of Cu-based anode-free full cells at different cycles were compared across the three cathode mass loadings to diagnose capacity degradation (**Figure 6A**). The cell with a 15 mg cm^{-2} cathode delivered a discharge capacity of 133.7 mAh g^{-1} with the highest ICE of 92.1%, while the cell with a 5 mg cm^{-2} cathode showed a lower discharge capacity of 122.7 mAh g^{-1} with the lowest ICE of 88.3%. This indicates that less Li was stripped back to the cathode in the low cathode loading cell, which is probably due to the incomplete plated Li coverage with voids on the CC. After 10 cycles, the discharge voltage in the cell with a 5 mg cm^{-2} cathode dropped abruptly from 3.84 to 3.0 V, indicating poor interfacial contact and significant dead Li formation at the end of the stripping process. In contrast, the cell with a 15 mg cm^{-2} cathode exhibited a more gradual decrease to 3.0 V in discharge voltage, with less dead Li remaining on the CC after stripping. The degradation caused by poor interfacial contact in the cell with a lower cathode mass loading became even more pronounced after 20 cycles.

Figure 6B presents galvanostatic charge/discharge profiles for Ni-based anode-free cells with varying cathode mass loadings. Similar to the Cu-based cells, the Ni-based cell with a higher cathode mass loading exhibits higher initial ICE and slower capacity degradation. Notably, in cells with a 5 mg cm^{-2} cathode, the discharge voltage after 10 cycles shows a sharp drop from 3.9 to 3.0 V, while in cells with a 15 mg cm^{-2} cathode, the voltage decline is more gradual. This rapid voltage drop in cells with lower cathode mass loading suggests poor interfacial contact and significant dead Li formation at the end of the stripping process. For Au-seeded anode-free full cells, increasing the cathode mass loading similarly enhances cycling stability, with higher mass loadings resulting in slower capacity degradation, as shown in

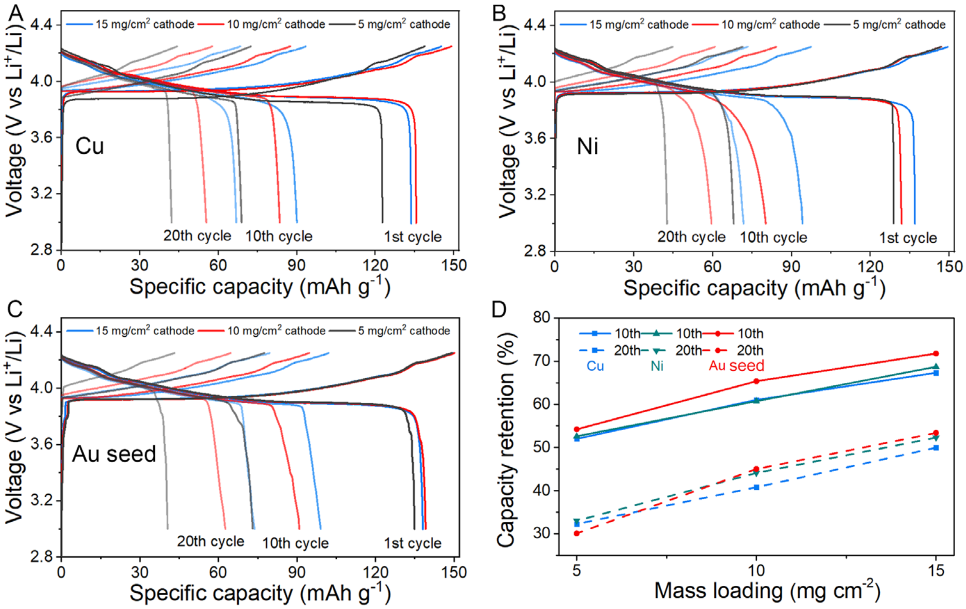

Figure 6. Electrochemical performance of anode-free full cells with different mass loading of cathode materials (5, 10, and 15 mg cm^{-2}). A) Galvanostatic charge/discharge profiles of the Cu-based anode-free full cells cycled with different cathode mass loadings. B) Galvanostatic charge/discharge profiles of the Ni-based anode-free full cells cycled with different cathode mass loadings. C) Galvanostatic charge/discharge profiles of the Au seed-based anode-free full cells cycled with different cathode mass loadings. D) Capacity retention comparison after 10, and 20 cycles among different cathode mass loadings. All cells were cycled at 0.25C at room temperature.

Figure 6C. Electrochemical measurements were conducted on at least two independent cells to ensure that the experiments were reproducible (Figure S14, Supporting Information). Figure 6D compares the capacity retention across different cathode mass loadings after 10 and 20 cycles, clearly illustrating that low cathode mass loading hinders capacity retention in solid-state anode-free cells: a trend opposite to that observed in conventional solid-state batteries with excess Li metal anodes. The cell with Au-seed shows a slightly higher capacity retention than that of the cell with Ni and Cu at a higher cathode mass loading. However, at a lower cathode mass loading of 5 mg cm^{-2}, the cell with Au-seed exhibits a poorer capacity retention compared to cells with Cu and Ni. This is likely due to the LiAu alloying/dealloying processes, which consume additional Li with each cycle. As a result, the limited Li supply from the low mass loading cathode is gradually reduced over multiple cycles.

The investigation of cathode mass loading effects in AFSSBs reveals a counterintuitive phenomenon that challenges the conventional understanding of solid-state battery design. While traditional solid-state Li-metal batteries benefit from low cathode loading due to minimal volume variation and better kinetics, based on this study, the anode-free cells demonstrate an opposite trend due to the complex interplay between Li supply and interfacial dynamics. Higher cathode mass loadings (15 mg cm^{-2}) enable more complete and uniform Li coverage on current collectors, resulting in superior ICE (92.1% vs 88.3%) and sustained interfacial contact during cycling. This behavior manifests differently across current collector materials: Cu and Ni systems show similar degradation patterns tied to interfacial contact loss, while Au systems exhibit accelerated capacity fade in low-loading configurations due to competing Li-Au alloying reactions. This mass loading-dependent performance reveals a fundamental trade-off between Li supply adequacy and interfacial stability—higher loadings provide sufficient Li ions to maintain stable interfaces and uniform coverage, while lower loadings lead to incomplete coverage, poor interfacial contact, and accelerated dead Li formation, ultimately governing the cell's electrochemical stability. To verify our hypothesis regarding the effect of cathode mass loading on the anode, SEM analysis was conducted to examine the surface morphology of the anode at 30% SOC under different cathode mass loadings. The SEM image for the 5 mg cm^{-12} cathode reveals a small number of large, discontinuous particles with a light white appearance, whereas the SEM images for the 10 and 15 mg cm^{-2} cathodes display a greater number of smaller particles with a dark black appearance that are more evenly distributed (Figure S15, Supporting Information). Enlarged SEM images for the 10 and 15 mg cm^{-2} cathodes further reveal a significant number of small, light white particles attached to the dark black particles.

Low-magnification SEM-EDX mapping indicates that the light-colored particles are LPSC particles adhered to the anode (Figure S16, Supporting Information). Notably, the deposited Li on the CC is sticky, allowing LPSC particles to easily adhere during the peeling of the anode current collector. A comparison of Cu element mapping images reveals that, for the 5 mg cm^{-2} cathode, the Cu surface exhibits low coverage by both deposited Li and adhered LPSC particles, with noticeable gaps in the coverage where the Cu surface remains exposed (**Figure** 7A,B). In contrast, the Cu surfaces with 10 mg cm^{-2} (Figure 7C,D) and 15 mg cm^{-2} (Figure 7E,F) cathodes exhibit significantly higher coverage, particularly for the 15 mg cm^{-2} cathode, where most areas are covered by either LPSC particles or deposited Li (Figure S16, Supporting Information). As discussed previously, O element mapping was employed to track deposited Li. For the 5 mg cm^{-2}

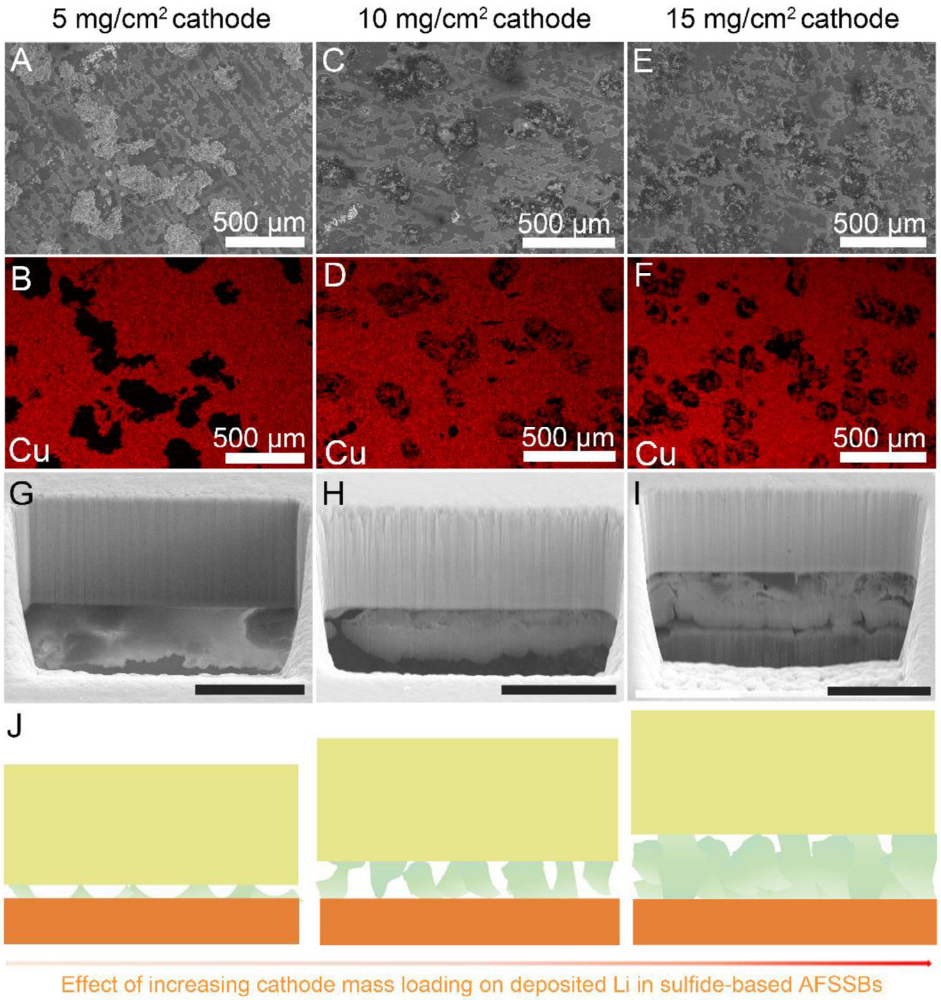

Figure 7. Top-view SEM and EDX-mappings of the deposited Li on Cu CCs at 30 SOC% under different cathode mass loadings. A,B) 5 mg cm^{-2} cathode mass loading; C,D) 10 mg cm^{-2} cathode mass loading; E,F) 15 mg cm^{-2} cathode mass loading; In the EDX mapping images, the red color represents the area of Cu, while the black areas represent the deposited Li covering the Cu CCs. FIB cross-sectional SEM of the deposited Li at 100 SOC% under different cathode mass loadings. G) 5 mg cm^{-2} cathode mass loading; H) 10 mg cm^{-2} cathode mass loading; I) 15 mg cm^{-2} cathode mass loading. The scale bar is 10 µm. J) Schematic illustration of effect of increasing cathode mass loading on deposited Li in AFSSBs.

cathode, the O element mapping shows minimal intensity, as most of the deposited Li is buried beneath LPSC particles. However, for the 15 mg cm^{-2} cathode, the O element mapping reveals distinct intensity differences, indicating more uniform coverage of the current collector (Figure S16, Supporting Information). High-magnification EDX mapping of the Cu with 15 mg cm^{-2} cathode confirms the absence of LPSC particles on the dark black deposits, while the O element mapping shows strong intensity at these locations, suggesting that the dark black deposits are deposited Li (Figure S17, Supporting Information).

To further confirm the effect of increasing cathode mass loading on Li deposition in sulfide-based AFSSBs, focused ion beam (FIB)-SEM was used to analyze the cross-sectional morphologies of deposited Li at 100% SOC under different cathode mass loadings. For the 5 mg cm^{-2} cathode sample, a 20 µm × 25 µm area was randomly milled. As shown in Figure S18 (Supporting Information), no Li was observed directly beneath the CC in this region, indicating that no Li was plated at the CC/solid electrolyte (SE) interface. Upon milling another area, an obvious deposition layer appeared below the CC, with large voids still present at the CC interface (Figure 7G). As evidenced by Figure 7G and Figure S18 (Supporting Information), the Li deposition is non-uniform and has a low coverage on the CC when the mass loading is 5 mg cm^{-2}. In contrast, for the 10 mg cm^{-12} cathode sample, a randomly milled area revealed a deposited Li layer beneath the CC (Figure 7H), with relatively uniform coverage and only a few small voids observed at the CC interface. At 15 mg cm^{-2}, a thicker deposited Li layer was observed beneath the CC (Figure 7I), suggesting increased Li deposition. Although small voids were still present, the deposition thickness across the milled region was more uniform compared to the 10 mg cm^{-2} sample, where the right-side thickness was smaller. Another milled area also revealed a thick deposited Li layer with a few small voids at the CC interface (Figure S19, Supporting Information), indicating improved anode CC coverage with 15 mg cm^{-2} cathode mass loading. It should be noted that FIB milling provides localized structural insights due to its small sampling area. Therefore, by combining large-area top-view SEM and corresponding EDX mappings with FIB cross-sectional SEM images, we can conclude that increasing cathode mass loading not only enhances Li deposition thickness but also promotes a higher Li deposition coverage on the CCs (Figure 7J).

3. Conclusion

In summary, this work identifies a key finding: the critical role of cathode mass loading (as the Li^+ source) in anode-free solid-state batteries, which contrasts with the behavior of solid-state batteries employing Li metal anodes. While Li metalbased solid-state batteries benefit from minimal cathode loading to mitigate mechanical issues such as Li creeping, we found that AFSSBs require a sufficiently large Li^+ reservoir (15 mg cm^{-2} in this study) to maintain stable anode/solid-electrolyte interfacial dynamics during cycling. This requirement stems from the fundamental need for complete electrode coverage: when the Li^+ supply is insufficient, heterogeneous nucleation and growth occur, producing electrochemically isolated domains that accelerate performance degradation.

Meanwhile, through cryo-TEM investigations, we also investigated the nanoscale mechanisms governing electrochemically derived "fresh" Li evolution in sulfide-based AFSSBs. Our studies reveal three distinct substrate-dependent growth dynamics: 1) Cu promotes heterogeneous nucleation, leading to dendritic evolution with concurrent formation of interfacial species (Li_2S/LiCl); 2) Ni enables homogeneous growth resulting in non-dendritic film morphologies; and 3) Au exhibits unique behavior through formation of a critical alloy interlayer before Li plating. Furthermore, we investigated the current density effect on Li deposit morphology: high rates (0.25C) drive nucleation-dominated growth, producing numerous small deposits, while low rates (0.04C) enable diffusion-controlled evolution, forming thermodynamically favored larger structures. These discoveries establish three foundational principles for AFSSBs development: interfacial chemistry optimization through selective substrate engineering, nucleation control via kinetic modulation, and electrochemical stability through sufficient Li^+ supply. While this study focuses on experimental analysis of Li nucleation and growth behavior, detailed kinetic modeling is beyond the scope of this work and will be explored in future work. These understandings bridge the gap between nanoscale phenomena and device-level performance, providing scientific guidelines for practical high-energy-density AFSSBs for real-world applications.

4. Experimental Section

Materials Preparation: $Li_{5.4}PS_{4.4}Cl_{1.6}$ (LPSC) was synthesized via a mechanical ball-milling process followed by an annealing process.[33] To be specific, lithium sulfide (Li_2S,99.98%, Sigma–Aldrich), phosphorus pentasulfide (P_2S_5, 99%, Sigma–Aldrich), and lithium chloride (LiCl, >99.98%, Sigma–Aldrich) were stoichiometrically mixed manually in an agate motor, the mixed powders were then transferred into in a stainless-steel jar in an Ar glovebox and ball-milled at 500 rpm for 40 cycles. After ball-milling, the mixture was sealed in a glass tube under vacuum and annealed at 510 °C for 2 h with a heating rate of 5 °C min^{-1}.

Li_2SiO_x-coated $LiCoO_2$ (LCO, Sigma–Aldrich): LCO was used as a model cathode to study Li deposition/stripping behaviors in AFSSBs. A wet-chemical method was used to coat a thin layer of Li_2SiO_x on LCO particles to eliminate the interface reaction with LPSC.[34]

Anode-Free Cell Fabrication: Asymmetric anode-free half-cells were fabricated by first loading 127 mg of SE powders into a PEEK die with a diameter of 12.7 mm and cold pressing them at 410 MPa to form a pellet. A piece of 10 mm In, 10 mm Li, and 12.7 mm copper disc foils was sequentially placed on one side of the SE pellet and cold pressed at a gradually increased pressure of ≈20 MPa for 1 min to improve the physical contact at the LiIn/SE interface. Next, a 12.7 mm diameter disc metal foil (Cu foil, Ni foil, and 20 nm Au-coated stainless steel (SS) foil) was placed on the other side of the SE pellet, followed by loading a piece of carbon felt. The cell was then positioned in a home-made frame, and an external pressure of 7.5 MPa was applied using a torque wrench during the cell testing. Anode-free full cells were assembled using a slightly modified procedure for the half cells. Specifically, 127 mg of SE powders were loaded into the PEEK die and pelletized at a low pressure of 40 MPa. The cathode composites, prepared by hand-mixing Li_2SiO_x-coated LCO, SE, and graphited carbon nanofiber (GCNF) in a weight ratio of 75:24:1, were then loaded on one side of the SE pellet and compressed with a 12.7 mm diameter steel pillar by hand. The cell stack was then pressed at a high pressure of 410 MPa to densify the two layers. Afterward, a 12.7 mm diameter of disc metal foil (Cu foil, Ni foil, and 20 nm Au-coated stainless steel (SS) foil) or metal grids (Cu, Ni, and Au) was placed on the other side of the SE pellet, followed by loading a piece of carbon felt. The cell was then positioned in a home-made frame, and an external pressure of 7.5 MPa was applied by using a torque wrench during the cell testing.

Electrochemical Characterization: Electrochemical measurements were conducted inside the Ar-filled glovebox to avoid air exposure. For the anode-free half cells, the cutoff voltage during the stripping process was set to 0.2 V. The electrochemical performance of the anode-free full cells was tested within the voltage range of 3.0–4.25 V versus Li^+/Li. All the electrochemical measurements were performed on a Landt battery cycler or a BioLogic cycler. All experiments were conducted at 25 °C.

Cryo-TEM Sample Preparation and Cryo-Transfer Procedure: To prepare TEM samples for cryo-TEM, the anode-free full cell was assembled in a standard mold cell using a TEM grid (Cu, Ni, or Au mesh, Ted Pella) as the substrate. After performing Li deposition/stripping, the mold cell was disassembled in a glovebox, and the metal grid was collected and placed in a 1.5 mL plastic tube. The sealed plastic tube was then plunged directly into a liquid nitrogen bath and quickly crushed with a cutter while the TEM grid remained immersed in the liquid nitrogen. The TEM grid was swiftly transferred into a cryo-transfer TEM holder, and a specialized shutter on the holder was immediately closed to prevent air exposure. The TEM sample was maintained at cryogenic temperatures during the following characterizations.

Materials Characterization: The scanning electron microscopy (SEM) morphologies of the deposited Li and energy-dispersive X-ray spectroscopy (EDS) were acquired with a Hitachi S4800 scanning electron microscope set at 3 kV. High-angle annular dark-field scanning transmission electron microscopy (HAADF-STEM) image was performed using the FEI Talos F200X operating at 200 kV. The microscope was equipped with a super EDS detector for elemental mapping.

Supporting Information

Supporting Information is available from the Wiley Online Library or from the author.

Acknowledgements

H.Z. acknowledges the financial support received from the Office of Science Department of Energy under Award Number DESC0024528. Work performed at the Center for Nanoscale Materials, a U.S. Department of Energy Office of Science User Facility, was supported by the U.S. DOE, Office of Basic Energy Sciences, under Contract No. DE-AC02-06CH11357.

The authors also thank Prof. Kenneth S. Burch and Michael Geiwithz from Boston College for their help on Au deposition on SS foils.

Conflict of Interest

The authors declare no conflict of interest.

Author Contributions

H.Z. supervised this work. J.W. performed electrochemical and cryo-TEM characterizations. Y.L. and G.W. helped with the cryo-TEM measurements. M.Y. and C.X. helped with the schematic Figure drawing. J.W. wrote the manuscript. All the authors contributed to the discussion of the manuscript.

Data Availability Statement

The data that support the findings of this study are available from the corresponding author upon reasonable request.

Keywords

anode-free solid-state batteries, cryo-transmission electron microscopy (Cryo-TEM), fresh lithium, interfacial chemistry, lithium nucleation and growth

Received: May 30, 2025
Revised: August 20, 2025
Published online:

---

[1] L. Zhou, N. Minafra, W. G. Zeier, L. F. Nazar, *Acc. Chem. Res.* **2021**, *54*, 2717.
[2] C. Yu, L. van Eijck, S. Ganapathy, M. Wagemaker, *Electrochim. Acta* **2016**, *215*, 93.
[3] Q. Zhang, D. Cao, Y. Ma, A. Natan, P. Aurora, H. Zhu, *Adv. Mater.* **2019**, *31*, 1901131.
[4] K. H. Park, Q. Bai, D. H. Kim, D. Y. Oh, Y. Zhu, Y. Mo, Y. S. Jung, *Adv. Energy Mater.* **2018**, *8*, 1800035.
[5] S. Chen, J. Zhang, L. Nie, X. Hu, Y. Huang, Y. Yu, W. Liu, *Adv. Mater.* **2021**, *33*, 2002325.
[6] D. H. Liu, Z. Bai, M. Li, A. Yu, D. Luo, W. Liu, L. Yang, J. Lu, K. Amine, Z. Chen, *Chem. Soc. Rev.* **2020**, *49*, 5407.
[7] C. Zor, S. J. Turrell, M. S. Uyanik, S. Afyon, *Adv. Energy Sustain. Res.* **2023**, *5*, 2300001.
[8] S. E. Sandoval, C. G. Haslam, B. S. Vishnugopi, D. W. Liao, J. S. Yoon, S. H. Park, Y. Wang, D. Mitlin, K. B. Hatzell, D. J. Siegel, P. P. Mukherjee, N. P. Dasgupta, J. Sakamoto, M. T. McDowell, *Nat. Mater.* **2025**, *62*, 9370.
[9] J. Wang, H. Zhu, *ACS Energy Lett.* **2025**, *10*, 2377.
[10] M. A. Thorpe, M. Zhang, D. W. Liao, S. E. Sandoval, Y. Kim, M. T. McDowell, M. D. Thouless, N. P. Dasgupta, *Matter* **2025**, *8*, 101955.
[11] J. H. Lee, S.-H. Oh, H. Yim, H.-J. Lee, E. Kwon, S. Yu, J. S. Kim, J. Song, J. Koo, J. Cho, S. H. Kim, A. Ryu, S. H. Choi, Y. Kim, G. Im, J.-W. Choi, S.-H. Yu, *Energy Storage Mater.* **2024**, *69*, 103398.
[12] D. Jun, S. H. Park, J. E. Jung, S. G. Lee, K. S. Kim, J. Y. Kim, K. Y. Bae, S. Son, Y. J. Lee, *Adv. Funct. Mater.* **2023**, *34*, 2310259.
[13] Y. Wang, Y. Liu, M. Nguyen, J. Cho, N. Katyal, B. S. Vishnugopi, H. Hao, R. Fang, N. Wu, P. Liu, P. P. Mukherjee, J. Nanda, G. Henkelman, J. Watt, D. Mitlin, *Adv. Mater.* **2023**, *35*, 2206762.
[14] J. Lee, S. H. Choi, G. Im, K. J. Lee, T. Lee, J. Oh, N. Lee, H. Kim, Y. Kim, S. Lee, J. W. Choi, *Adv. Mater.* **2022**, *34*, 2203580.
[15] S. E. Sandoval, J. A. Lewis, B. S. Vishnugopi, D. L. Nelson, M. M. Schneider, F. J. Q. Cortes, C. M. Matthews, J. Watt, M. Tian, P. Shevchenko, P. P. Mukherjee, M. T. McDowell, *Joule* **2023**, *7*, 2054.
[16] D. Spencer-Jolly, V. Agarwal, C. Doerrer, B. Hu, S. Zhang, D. L. R. Melvin, H. Gao, X. Gao, P. Adamson, O. V. Magdysyuk, P. S. Grant, R. A. House, P. G. Bruce, *Joule* **2023**, *7*, 503.
[17] Y. Wang, V. Raj, K. G. Naik, B. S. Vishnugopi, J. Cho, M. Nguyen, E. A. Recker, Y. Su, H. Celio, A. Dolocan, Z. A. Page, J. Watt, G. Henkelman, Q. H. Tu, P. P. Mukherjee, D. Mitlin, *Adv. Mater.* **2025**, *37*, 2410948.
[18] S. H. Park, K. G. Naik, B. S. Vishnugopi, P. P. Mukherjee, K. B. Hatzell, *Adv. Energy Mater.* **2024**, *15*, 2405129.
[19] S. Wenzel, S. J. Sedlmaier, C. Dietrich, W. G. Zeier, J. Janek, *Solid State Ion.* **2018**, *318*, 102.
[20] M. Li, B. Wang, J. Ma, Z. Wang, Y. Liang, Z. Wang, L. Zhang, Y. Tang, Q. Huang, J. Huang, *Adv. Energy Mater.* **2023**, *14*, 2303156.
[21] R. Lin, Y. He, C. Wang, P. Zou, E. Hu, X. Q. Yang, K. Xu, H. L. Xin, *Nat. Nanotechnol.* **2022**, *17*, 768.
[22] J. Wang, W. Huang, A. Pei, Y. Li, F. Shi, X. Yu, Y. Cui, *Nat. Energy* **2019**, *4*, 664.
[23] B. Han, X. Li, Q. Wang, Y. Zou, G. Xu, Y. Cheng, Z. Zhang, Y. Zhao, Y. Deng, J. Li, M. Gu, *Adv. Mater.* **2022**, *34*, 2108252.
[24] X. Xing, Y. Li, S. Wang, H. Liu, Z. Wu, S. Yu, J. Holoubek, H. Zhou, P. Liu, *ACS Energy Lett.* **2021**, *6*, 1831.
[25] L. Ye, Y. Lu, Y. Wang, J. Li, X. Li, *Nat. Mater.* **2024**, *23*, 244.
[26] P. Bach, I. Valencia-Jaime, U. Rütt, O. Gutowski, A. H. Romero, F. U. Renner, *Chem. Mater.* **2016**, *28*, 2941.
[27] P. Bach, M. Stratmann, I. Valencia-Jaime, A. H. Romero, F. U. Renner, *Electrochim. Acta* **2015**, *164*, 81.
[28] F. Sagane, K.-i. Ikeda, K. Okita, H. Sano, H. Sakaebe, Y. Iriyama, *J. Power Sources* **2013**, *233*, 34.
[29] S. H. Park, Y. J. Lee, *J. Mater. Chem. A* **2021**, *9*, 1803.
[30] Z. Zhang, X. Zhou, Z. Liu, *J. Alloys Compd.* **2022**, *893*, 162389.
[31] T. Fuchs, J. Becker, C. G. Haslam, C. Lerch, J. Sakamoto, F. H. Richter, J. Janek, *Adv. Energy Mater.* **2022**, *13*, 2203174.
[32] Z. Wang, Z. Mu, T. Ma, W. Yan, D. Wu, Y. Li, M. Yang, J. Peng, Y. Xia, S. Shi, L. Chen, H. Li, F. Wu, *Adv. Energy Mater.* **2024**, *14*, 2400003.
[33] X. Sun, D. Cao, Y. Wang, T. Ji, W. Liang, H. Zhu, *Adv. Mater. Interfaces* **2022**, *9*, 2200539.
[34] D. Cao, X. Sun, Y. Li, A. Anderson, W. Lu, H. Zhu, *Adv. Mater.* **2022**, *34*, 2200401.